

Direct Quantification of Serum Protein Interactions with PEGylated Micelle Nanocarriers

D. Paul Mallory,[⊥] Abegel Freedman,[⊥] Megan J. Kaliszewski, Gladys Rocío Montenegro-Galindo, Coleen Pugh, and Adam W. Smith*



Cite This: *Biomacromolecules* 2023, 24, 2479–2488



Read Online

ACCESS |



Metrics & More

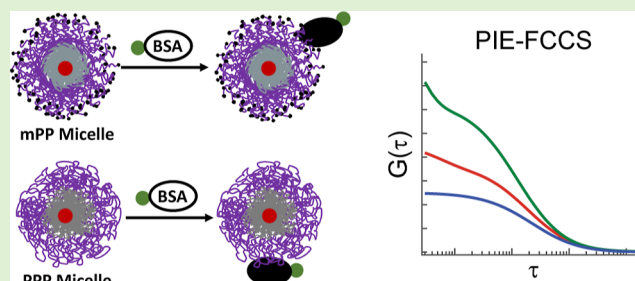


Article Recommendations



Supporting Information

ABSTRACT: A large repertoire of nanocarrier (NC) technologies exists, each with highly specified advantages in terms of targetability, stability, and immunological inertness. The characterization of such NC properties within physiological conditions is essential for the development of optimized drug delivery systems. One method that is well established for reducing premature elimination by avoiding protein adsorption on NCs is surface functionalization with poly(ethylene glycol) (PEG), aptly called PEGylation. However, recent studies revealed that some PEGylated NCs have a delayed immune response, indicating the occurrence of protein-NC interactions. Obvious protein-NC interactions, especially in micellar systems, may have been overlooked as many early studies relied on techniques less sensitive to molecular level interactions. More sensitive techniques have been developed, but a major challenge is the direct measurement of interactions, which must be done in situ, as micelle assemblies are dynamic. Here, we report the use of pulsed-interleaved excitation fluorescence cross-correlation spectroscopy (PIE-FCCS) to interrogate the interactions between two PEG-based micelle models and serum albumin protein to compare protein adsorption differences based on linear or cyclic PEG architectures. First, by measuring micelle diffusion in isolated and mixed solutions, we confirmed the thermal stability of diblock and triblock copolymer micelle assemblies. Further, we measured the co-diffusion of micelles and serum proteins, the magnitudes of which increased with concentration and continued incubation. The results demonstrate that PIE-FCCS is capable of measuring direct interactions between fluorescently labeled NC and serum proteins, even at concentrations 500 times lower than those observed physiologically. This capability showcases the potential utility of PIE-FCCS in the characterization of drug delivery systems in biomimetic conditions.



INTRODUCTION

Poly(ethylene glycol)'s (PEG's) antifouling property has revolutionized the drug delivery field, where it is widely accepted that PEGylation increases the blood circulation time of hydrophobic therapeutics.^{1–7} The general mechanism by which PEGylation achieves this increased circulation time is by avoiding protein adsorption and the ensuing endogenous defense mechanisms. Consequently, PEG is now commonly described as imparting a “stealth” characteristic to protein and drug delivery devices. However, this descriptor is misleading. Studies have found that colloidal PEGylated drug delivery systems can be rapidly eliminated upon subsequent doses, known as the accelerated blood clearance (ABC) phenomenon,^{8–12} which has been attributed to an immune response mediated by complement activation,^{6,13,14} and the production of anti-PEG antibodies.^{12,15–17} A number of groups have reported that the extent of the immune response depends on slight changes in molecular weight,⁹ hydrophobic polymer blocks,¹¹ and even the hydrophobicity of payloads.¹⁸ However, after studying a range of different PEGylated micelles, Yokoyama et al. did not find a consistent trend that can be

used to predict immunological responses in future compositions of PEGylated polymers and micelles.^{10,19} These observations are evidence for direct protein–micelle interactions and suggest that quantitative studies are needed to measure the affinity and kinetics of the possibly weak, and therefore difficult to detect, interactions in vitro and in situ. By doing this, connections can be made between protein–micelle interactions that occur before the anti-PEG antibody induction and the corresponding degree of ABC after its induction. Currently, the most common way to detect anti-PEG antibody production involves in vivo administration of therapeutics and the subsequent serum analysis of stimulated antibodies using enzyme-linked immunosorbent assays (ELISAs). A major advantage of ELISA is its sensitivity and ability to directly

Received: December 30, 2022

Revised: May 6, 2023

Published: May 24, 2023



measure binding. However, a limitation of ELISA is that it cannot detect in situ micelle–protein interactions. The limiting factor occurs during the ELISA protocol, which requires the washing of the wells to remove any unbound species from the detection surface. The washes would certainly drive the micelles below the critical micelle concentration (CMC), thereby disrupting the micelle structure. It is possible to anchor the polymeric component of a PEGylated micelle; however, the chemical environment of the anchors artificially affects binding with anti-PEG antibodies.²⁰ This raises questions about the conclusion that anti-PEG antibodies recognize not only the PEG main chain but also the interface between the PEG and the hydrophobic blocks in the polymer.¹⁰ Other techniques utilizing localized surface plasmon resonance and the detection of equilibrium fluctuations have been employed.²⁰ However, these techniques still rely on surface immobilization and therefore have the same limitations as ELISA.

To address the limitations inherent in ELISA and other assays that require surface immobilization, other studies have employed softer methods for measuring micelle stability and interactions in the presence of serum proteins. Studies using classic ensemble methods, such as UV–vis, have investigated PEGylated micelle stability in the presence of bovine serum albumin (BSA) by monitoring turbidity changes; however, this is a qualitative technique that requires enough binding to induce micelle aggregation.²¹ Additional work partially bridges the gap between ensemble and single-molecule studies by incorporating dynamic light scattering (DLS) in their exploration of the micelle–BSA interactions.^{5,22} While these findings have provided some insight into the types of micelles that aggregate in the presence of BSA, they are still limited in the level of resolution by which they can probe weak and specific interactions that are low in concentration.

The fluorescent analogue of DLS, fluorescence correlation spectroscopy (FCS), has proven to be sensitive to subtle changes in nanocarrier (NC) systems under different conditions.^{23–25} FCS is unique in its ability to correlate photon emissions with single-molecule sensitivity as they migrate through a femtoliter confocal excitation volume, ultimately enabling the detection of discrete size and population variations.²⁶ Protein–NC interactions have been studied using FCS by detecting changes in diffusion and therefore size,²⁴ but a disadvantage of using this technique is the inability to distinguish self-aggregation, which can lead to false positive results. This disadvantage can be overcome with fluorescence cross-correlation spectroscopy (FCCS), which simultaneously measures diffusivity and local concentrations of the protein and NC populations as well as the population of bound, co-diffusing species.²⁷ Recent work has demonstrated the capabilities of FCCS to characterize single-molecule level interactions between metal–organic framework (MOF) nanoparticles and strongly binding serum proteins.²⁸ In this study, we used FCCS to directly measure the interactions between micellar NCs with diblock and triblock (m)PEG-polycaprolactone (PCL) topologies and a nonspecific serum protein, BSA. This approach enables the quantification of weak protein–micelle interactions and sets the stage to optimize the effects of micellar architecture on micelle structural stability on serum protein binding, a critical aspect of NC design.

MATERIALS AND METHODS

Materials. Materials used as received included acetone (Sigma-Aldrich, 99.5%), BSA-FITC (fluorescein isothiocyanate) (A23015, Thermo Fisher Scientific), Nile Red (Santa Cruz Biotech), PCL_{5k}-PEG_{10k}-PCL_{5k} (Sigma-Aldrich), and tin(II) 2-ethylhexanoate (Sigma-Aldrich, 94%). ϵ -Caprolactone (Acros Organics, 99%) was distilled from CaH₂ under reduced pressure. mPEG_{5k} (Aldrich) was azeotropically dried using toluene. 10× Phosphate-buffered saline (PBS, Lonza) was diluted to 1× PBS using MilliQ ultrapure water, and, if necessary, pH was adjusted to 7.4 with 3 M HCl and/or 0.5 M NaOH. Toluene (EMD, 99.5%) was dried by distillation from sodium benzophenone ketyl under N₂. Dialysis was performed using bags with a nominal molecular weight cut-off of 3500 Da (Fisher). All solutions were filtered through 0.22 μ m hydrophilic poly(vinylidene difluoride) (PVDF) filters (Aura MT).

Polymerization of ϵ -Caprolactone. ϵ -Caprolactone was polymerized under bulk conditions by adding tin(II) 2-ethylhexanoate (22 mg, 54 μ mol), mPEG_{5k} macroinitiator (0.54 g, 0.11 mmol), and ϵ -caprolactone monomer (1.9 g, 16 mmol) to a Schlenk tube inside a nitrogen-filled dry box.²⁹ The Schlenk tube was capped with a glass stopper, removed from the dry box, and heated to 110 °C while stirring for 30 min. The polymerization was stopped by quenching the Schlenk tube in liquid N₂ and opening it to the atmosphere. mPEG-PCL polymer was purified by diluting the polymerization mixture in CH₂Cl₂ (7 mL) and precipitating it in hexanes (70 mL) twice to yield a powdery white solid (1.2 g, 50%). Monomer conversion was determined to be 47% by ¹H NMR spectroscopy of an aliquot before precipitation. GPC_{ps}: M_n = 13.1 kDa, D = 1.20. ¹H NMR (300 MHz): δ 1.38 (m, $-CH_2CH_2CH_2OC=O-$), 1.65 (m, $-CH_2CH_2CH_2CH_2OC=O-$), 2.31 (t, $-OC=OCH_2-$), 3.38 (s, CH_3O-), 3.65 (s, $-OCH_2CH_2-$ and $-CH_2OH$, 448H), and 4.06 (t, $-CH_2OC=O-$).

Assembly of mPEG-PCL Micelles. Micelles were assembled using a combination of cosolvent evaporation and dialysis methods.³⁰ These methods were combined because, during model assembly studies, acetone persisted after solvent evaporation assisted by rotary evaporation. Acetone was detected by ¹H NMR spectroscopy after attempted solvent removal via rotary evaporation but was not detected after dialysis was performed instead of rotary evaporation. A typical assembly consisted of dissolving mPEG-PCL (10.5 mg, 0.802 μ mol) in acetone (860 μ L) and a 100 μ M acetone solution of Nile Red (NR) (140 μ L). This solution was added dropwise to 1× PBS (5.0 mL) and stirred uncovered under ambient temperature and pressure for 1 h. The solution was transferred to a dialysis bag and dialyzed against approximately 400 mL of 1× PBS. The solvent was exchanged 3× over 1.5 h with 1× PBS and was left in 1× PBS while stirring overnight after the final exchange. The resulting solution volume was measured and determined to be 6.4 mL, yielding a micelle concentration of 1.25 μ M. The concentration was adjusted with an additional 1× PBS to obtain a final micelle concentration of 0.25 \pm 0.06 μ M. The solution was filtered using 0.22 μ m hydrophilic PVDF filters before DLS, FCS, and pulsed-interleaved excitation FCCS (PIE-FCCS) characterization.

Assembly of PCL-PEG-PCL Micelles. Micelles were assembled using the same method as the mPEG-PCL micelles, except for concentration variations. A typical example involved dissolving PCL-PEG-PCL (5.4 mg, 0.27 μ mol) in acetone (1860 μ L) and a 100 μ M acetone solution of NR (140 μ L). The solution was then added dropwise to 1× PBS (5.0 mL) and stirred uncovered under ambient temperature and pressure for 4 h. The solution was transferred to a dialysis bag and dialyzed against approximately 400 mL of 1× PBS solution to remove a trace amount of acetone. The solvent was exchanged 3× over 1.5 h with 1× PBS solution. The dialysis bag was left in 1× PBS while stirring overnight after the final exchange. The resulting solution volume was measured and determined to be 6.2 mL, yielding a micelle concentration of 0.871 μ M. The concentration was adjusted with an additional 1× PBS to obtain a final micelle concentration of 0.25 \pm 0.06 μ M. The solution was filtered using 0.22

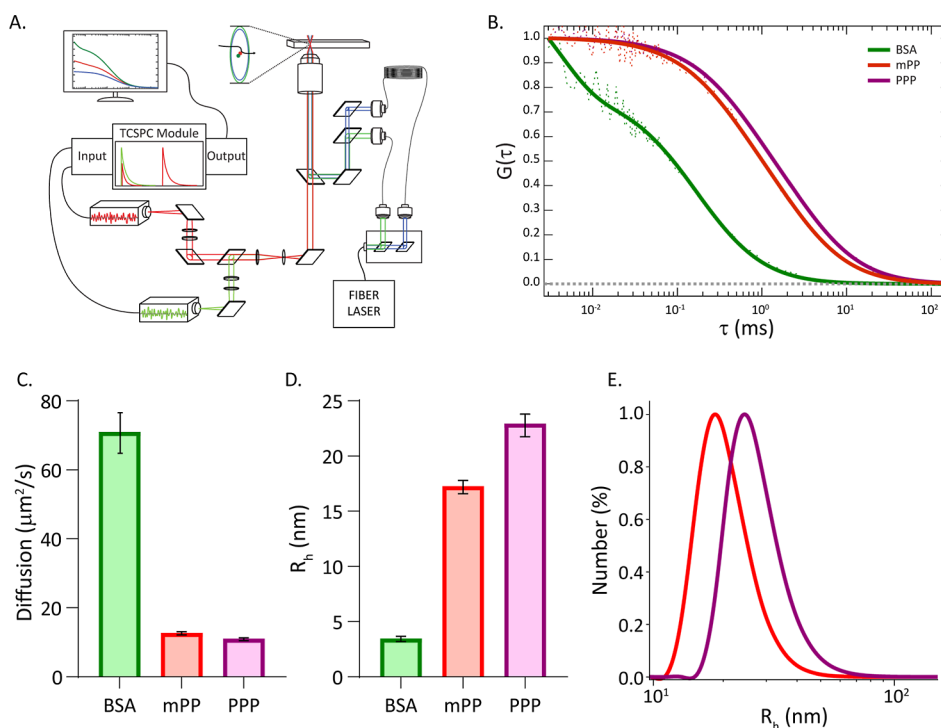


Figure 1. FCS characterization of isolated species in 1× PBS. (A) General diagram of the instrument setup and optical paths used for FCS measurements. (B) ACFs of sample data (dashed) and corresponding model fits (solid lines) of monomeric BSA (green), mPP (red), and PPP (violet) species. Average diffusion coefficients (C) and hydrodynamic radii (D) of monomers. Error bars show the standard deviation calculated for each sample. (E) Hydrodynamic radii populations of mPP (red) and PPP (violet) micelle samples from DLS experiments.

μm hydrophilic PVDF filters before DLS, FCS, and PIE-FCCS characterization.

DLS of Micelles. The sizes of mPEG-PCL and PCL-PEG-PCL micelles were measured directly after filtration, at the original concentration, under ambient temperature and pressure, by DLS using a Malvern Zetasizer Nano-ZS90.

Incubation of Micelles with BSA-FITC. Solutions of micelles alone and BSA alone were incubated at 37 °C in a temperature-controlled incubator and used as controls. To measure deviations from the controls, solutions with a mixture of micelles and BSA were also incubated at 37 °C. Concentrations were adjusted to be comparable with filtered 1× PBS.

Fluorescence Fluctuation Spectroscopy. Samples of BSA-FITC and micelle-NR solutions were either isolated or mixed at desired concentrations in Lo-Bind Eppendorf tubes (Eppendorf) and incubated at 37 °C in a temperature-controlled oven. After designated incubation times, sample aliquots were dispensed into a cleaned 96-well plate. This was then mounted onto our customized inverted microscope (Eclipse Ti, Nikon, Tokyo, Japan) for PIE-FCCS experiments, as previously described.^{31,32} The optical path is depicted in Figure 1A. Using dichroic mirrors and clean-up filters (LL01-488-12.5, Semrock, Rochester, NY/LL02-561-12.5, Semrock, Rochester, NY), we isolated excitation beams of 488 and 561 nm from a pulsed, supercontinuum fiber laser (SuperK NKT Photonics, Birkerød, Denmark). These beams were temporally separated by 50 ns by coupling them into identical 3 and 18 m single mode optical fibers, respectively. Upon exiting the fibers, the signals were adjusted to 4 μW using continuously variable neutral density filters (NDC-25C-4M, NDC-25C-2M, Thorlabs, Newton, NJ), before being spatially overlapped using a dichroic mirror (LM01-503-25, Semrock, Rochester, NY), and then directed into the posterior of the microscope. The excitation laser was directed into the optical path of the microscope with a laser filter cube (zt488/561 rpc and zet488/561 m, Chroma Technology, Bellows Falls, VT) and focused on the sample with a 100× oil-immersed objective (NA 1.49, Nikon, Tokyo, Japan). Emission from the sample was collected with the same objective and directed through a confocal detection assembly with a

50 μm pinhole. The fluorescence signal was spectrally separated with a dichroic mirror (FF560-FDi01-25 x 36, Semrock, Rochester, NY). The red (621 ± 34 nm) or green (520 ± 22 nm) emission signals were isolated with single bandpass filters (FF01-621/69-25, Semrock, Rochester, NY/FF01-520/44-25, Semrock, Rochester, NY). Individual photons were detected with two identical single-photon avalanche diodes (SPAD, Micro Photon Devices, Bolzano, Italy) and recorded with a four-channel routed time-correlated single-photon counting (TCSPC) device (PicoHarp 300, PicoQuant, Berlin, Germany).

PIE-FCCS Data Analysis. Experiments with the diblock and triblock micelles involved acquisition collections after incubating samples at 37 °C in a temperature-controlled oven for 1, 6, 12, 24, and 48 h. At each time, fluorescence fluctuation data were collected for 4 solutions, containing either BSA, micelle, micelle-1× BSA, or micelle-2× BSA. For each solution, TCSPC data were collected for ~20 min spread between 6 and 8 separate acquisitions, which were subsequently divided into 1 s sub-acquisitions. From the partitioned TCSPC data, the recorded photons were assigned to one of the two excitation sources based on their arrival times. Red and green photons detected within 40 ns following 561 and 488 nm excitation pulses were stored in arrays of 1 μs bins designated as fluorescent signals $F_R(t)$ and $F_G(t)$, respectively. Using a multiple-tau algorithm available in the PIE analysis with MATLAB (PAM) script repository,³³ we then calculated autocorrelation (ACF) or cross-correlation (CCF) functions using

$$G_{ij}(\tau) = \frac{\langle \delta F_i(t) \cdot \delta F_j(t + \tau) \rangle}{\langle F_i(t) \rangle \cdot \langle F_j(t) \rangle} \quad (1)$$

where $i = j$, being either R or G, for ACFs, $i \neq j$ for CCF, τ is lag time, and $\delta F(t) = F(t) - \langle F(t) \rangle$ with brackets denoting the time average. Aberrant correlation functions were removed based on divergence from population standard deviations before averaging the remaining sub-acquisitions. The final ACFs, $G_R(\tau)$ for micelles and $G_G(\tau)$ for isolated BSA, were fit in MATLAB using a weighted nonlinear least-squares algorithm to a single-component 3D diffusion with a blinking model function

$$G_i(\tau) = G(0) \cdot G_{3D \text{ diff}}(\tau) \cdot G_{\text{blink}}(\tau) \quad (2)$$

in which $G(0)$ is the function amplitude, defined as

$$G(0) = \frac{1}{\langle N_i \rangle} \quad (3)$$

where $\langle N_i \rangle$ equals the time-averaged number of fluorescent species found in the excitation volume. The 3D diffusion component $G_{3D \text{ diff}}(\tau)$ is defined as

$$G_{3D \text{ diff}}(\tau) = \frac{1}{1 + \frac{\tau}{\tau_{D,i}}} \cdot \frac{1}{\sqrt{1 + \frac{\tau}{\tau_{D,i}} \cdot \kappa^2}} \quad (4)$$

where $\tau_{D,i}$ is the average dwell time of species i diffusing through the confocal excitation volume, with an eccentricity factor κ from the wavelength-dependent axial (z_0) and lateral (ω_0) radii of the excitation volume. Lastly, the triplet blinking component, $G_{\text{blink}}(\tau)$, is

$$G_{\text{blink}}(\tau) = \frac{1 - T_i + T_i e^{-\tau/\tau_{T,i}}}{1 - T_i} \quad (5)$$

where T_i is the fraction of fluorescent species, i , occupying a dark triplet state, with a corresponding lifetime, $\tau_{T,i}$. When fitting cross-correlation data, $G_X(\tau)$, the blinking component was eliminated as $T = 0$. From the ACF fits, we use extracted dwell times to calculate diffusion coefficients as $D_i = \omega_0^2/4\tau_{D,i}$. The means and errors of the relevant output fit parameters for each acquisition were calculated, weighted by the number of sub-acquisitions used to calculate each final filtered acquisition. Using the experimentally measured diffusion coefficient of isolated BSA ($72.8 \pm 6.5 \mu\text{m}^2/\text{s}$), in good agreement with literature values,³⁴ we were able to correct for small (± 10 nm) variations in ω_0 from day to day.

When mixed with either micelle, the ACFs for BSA in solution were instead fit to a two-component 3D Brownian diffusion model with triplet blinking. The corresponding model equation is identical to that of the single component, but with $G_{3D \text{ diff}}(\tau)$ instead describing the sum of two species with distinguishable dwell times written as

$$G_{3D \text{ diff}}(\tau) = F_1 \left(\frac{1}{1 + \frac{\tau}{\tau_{D,G1}}} \cdot \frac{1}{\sqrt{1 + \frac{\tau}{\tau_{D,G1}} \cdot \kappa^2}} \right) + (1 - F_1) \left(\frac{1}{1 + \frac{\tau}{\tau_{D,G2}}} \cdot \frac{1}{\sqrt{1 + \frac{\tau}{\tau_{D,G2}} \cdot \kappa^2}} \right) \quad (6)$$

where F_1 is the fraction of species with dwell times $\tau_{D,G1}$ and the remaining species diffusing with average dwell times, $\tau_{D,G2}$. The overall average diffusion coefficients for such systems were then calculated as follows.

$$D_G = \frac{\omega_0^2}{4(F_1\tau_{D,G1} + (1 - F_1)\tau_{D,G2})} \quad (7)$$

Using the Stokes–Einstein equation, we then calculated the corresponding hydrodynamic radii as

$$R_h = \frac{k_B T}{6\pi\eta D_G} \quad (8)$$

where k_B is Boltzmann's constant, η is the viscosity assumed to be $9.3255 \times 10^{-4} \text{ kg/m}\cdot\text{s}$, and T is the temperature, taken as 296 K. Finally, we used the amplitudes from the green channel ACFs and the dual channel CCFs to generate a fractionally correlated metric, f_g , which describes the relative degree of adsorption and co-diffusion of spectrally distinct species, defined as follows.

$$f_g = \frac{G_{RG}(0)}{G_G(0)} \quad (9)$$

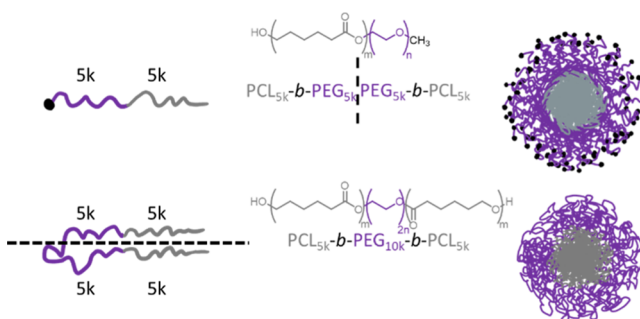
RESULTS AND DISCUSSION

Synthesis and Characterization of mPEG_{5k}-PCL_{6k}-mPEG with a reported number-average molecular weight (M_n) of 5.0 kDa was used as a macroinitiator in the ring-opening polymerization (ROP) of ϵ -caprolactone with tin(II) 2-ethylhexanoate.²⁹ The polymerization was terminated before reaching 50% monomer conversion to decrease the probability of transesterification side reactions. ¹H NMR spectroscopy was used to determine the monomer conversion and confirm the expected polymer structure (Figure S1). Gel permeation chromatography (GPC) with polystyrene standards was used to determine the macromonomer and final polymer's M_n and polydispersity (D). Prior to polymerization, the M_n of the mPEG macroinitiator was 7.01 kDa with $D = 1.08$. The final mPEG-PCL polymer had an M_n of 13.1 kDa with $D = 1.20$ (Figure S2). Therefore, the PCL chain length was determined to be 6.1 kDa, hence the mPEG_{5k}-PCL_{6k} notation.

Micelle Assembly, CMC, and Aggregation Number Determination. mPEG_{5k}-PCL_{6k} (mPP) and PCL_{5k}-PEG_{10k}-PCL_{5k} (PPP) micelles were assembled using the cosolvent evaporation method, as previously described.³⁰ However, trace amounts of acetone were detected using ¹H NMR spectroscopy. To remove the remaining acetone, dialysis was necessary. DLS was used to confirm the micelle size (Figure 1E) as well as the CMC (Figure S3). The hydrodynamic radius (R_h) values were measured to be 18.5 and 24.4 nm for mPP and PPP, respectively, and the CMC of mPP was determined to be 2.12 μM or 27.8 $\mu\text{g/mL}$, which agrees with the literature values.²² The aggregation number for mPP was measured using SLS (Figure S4) and resulted in an aggregation number of 100 polymers/micelle.

The PPP micelles were notably more difficult to form without aggregates. Due to the nature of triblock ABA copolymer micelle assemblies, dilute conditions were necessary to encourage the two hydrophobic ends to incorporate into the same micelle assembly as opposed to two different micelles, which is the major cause of aggregation. While they were prepared at half the concentration of the mPP micelles, they displayed similar sizes, as confirmed by DLS (Figure 1E) and transmission electron microscopy (TEM) (Figure S5). We, therefore, assumed the aggregation number for PPP is 50, as one triblock is equivalent to 2 diblocks (Scheme 1), which was necessary to calculate the micelle concentrations. The polymer concentration was maintained above 10 μM to ensure it did not fall below the CMC during the experiment. This was reasonable to assume, as ABA triblock copolymers have similar

Scheme 1. Illustration of Polymer Micelles Formed by mPEG-PCL (mPP) and PCL-PEG-PCL (PPP) in 1× PBS and Used in This Study



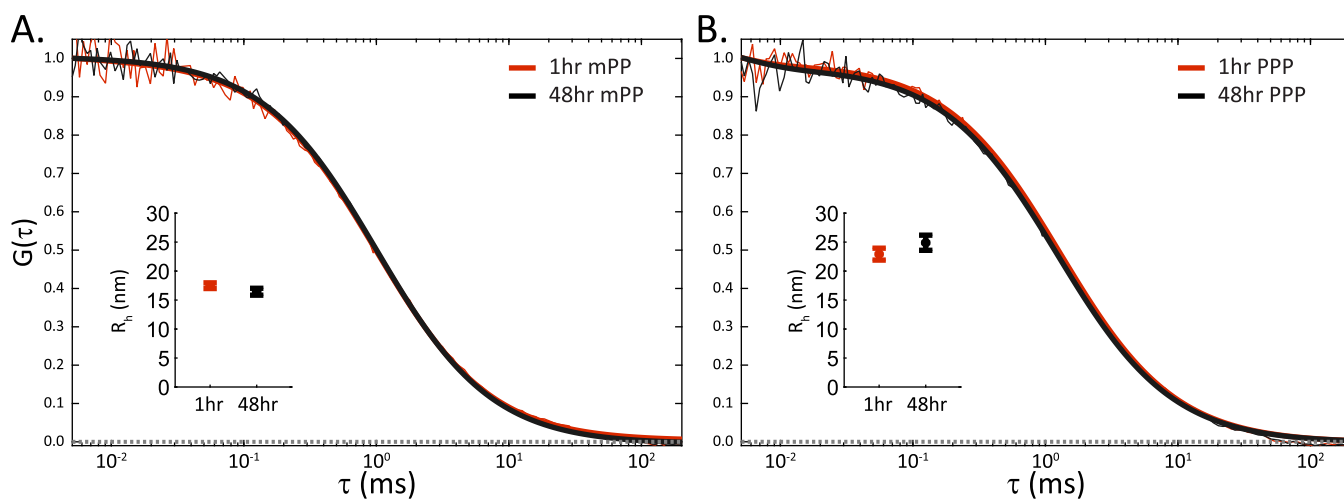


Figure 2. Micelle temperature stability with time. Representative, normalized sample ACFs of 342 nM solutions, containing NR-labeled mPP (A) and PPP (B) micelles after 1 h (red) and 48 h (black) incubations at 37 °C. Insets show R_h values corresponding to respective 1 and 48 h FCS measurements. Error bars show the standard deviations calculated for each sample.

CMCs to their diblock derivatives.^{5,35} Example calculations that relate polymer concentration to micelle concentration, as well as the dilution sequence for FCS and PIE-FCCS studies, can be found in the Supporting Information (Tables S1–S3).

Characterization of Micelles with FCS and DLS. To study the possible effects of end-groups on protein–micelle interactions, we used two different block copolymers: mPP and PPP. As illustrated in Scheme 1, the mPP micelles contain alkoxy (methoxy) end groups, whereas the PPP folds into hairpin-like loops when assembled into micelles, which eliminates the methoxy end groups. The appropriate M_n for the copolymer blocks in mPP was chosen based on the molecular weights of previously assembled stable micelles.³⁶ The M_n for the copolymer blocks in PPP was chosen to be comparable to the mPP blocks when PPP is folded. Because the M_n of the block copolymers is comparable when assembled into the micelles, we expect the micelle sizes to be comparable.

We first characterized the micelles and BSA prior to mixing using FCS, which can quantify the diffusion dynamics of a broad spectrum of sizes, ranging from fluorescent dyes (~1 nm) to micelles (10–30 nm) and liposomes (100–300 nm).^{37,38} BSA conjugated to FITC is commercially available and has a peak emission at 525 nm. NR (peak emission at 633 nm) was chosen as a fluorescent probe for the micellar solutions because it self-associates in the hydrophobic core of the micelles and is more fluorescent in that environment than in an aqueous solution.³⁹ Separate samples of FITC-labeled BSA and NR-labeled micelles were prepared at concentrations of 0.34 μM for BSA and $0.25 \pm 0.06 \mu\text{M}$ for mPP and PPP. Example calculations can be found in Table S2. Aliquots of micelle and BSA stock solutions were combined in 1:1 and 1:2 ratios of micelle/BSA (Table S2), which we refer to as 1 \times and 2 \times BSA mixtures, respectively. Additionally, BSA stock solutions were diluted by half in 1 \times PBS prior to measurements. Following preparation, the samples were incubated at 37 °C for time lengths of 1, 6, 12, 24, and 48 h. After each incubation period, 100 μL aliquots were taken from all samples and analyzed using single-color FCS. Data was recorded on an instrument setup shown in Figure 1A, yielding the ACFs shown in Figure 1B. As described in the Materials and Methods section, the ACFs were fit to a 3D diffusion model with triplet relaxation to determine τ_D , N , and T . Using the fit

values, we were able to quantify the micelle and BSA concentrations in isolated, 1 \times , and 2 \times mixtures, as reported in Table S3. The translational mobility of each species was compared using the diffusion coefficients, which were calculated from the respective τ_D values (Figure 1C).

The micelle mobilities were much lower than the BSA mobilities, which was expected based on their relative sizes. The diffusion coefficients of isolated mPP and PPP samples were 13.3 ± 0.4 and $10.2 \pm 0.4 \mu\text{m}^2/\text{s}$, respectively, making them nearly 7 times slower than BSA ($73.3 \pm 5.8 \mu\text{m}^2/\text{s}$, Figure 1C). Using the Stokes–Einstein equation, we then calculated the average R_h for mPP and PPP to be 17.5 ± 0.5 and 22.9 ± 1.0 nm, respectively (Figure 1D). The R_h calculated for mPP agrees with other studies performed using the same block copolymer with similar M_n s.^{22,40} The R_h calculated for PPP agrees with other studies performed using the same block copolymer and PCL/PEG ratio.^{35,41} The R_h calculated for BSA was 3.2 ± 0.2 nm, in good agreement with previous literature values,^{28,34,42,43} and indicates that isolated BSA samples existed primarily as monomeric species in these ~200 nM experimental concentrations. Additionally, we compared the R_h values of the micelles derived from FCS measurements to those from DLS measurements taken using aliquots from the same bulk micelle samples at room temperature. The DLS number data reported peak R_h values of 18.5 and 24.4 nm for mPP and PPP, respectively (Figure 1E), which agree very well with the R_h values from FCS.

We also tested the stability of both micelle types at physiologically relevant temperatures for extended periods of time. Such stability is essential for NCs to be considered potential candidates for drug delivery. We acquired FCS data for both micelle constructs after incubating isolated samples at 37 °C for both 1 and 48 h time points. Upon fitting the resulting ACFs, we observed consistent diffusion coefficients (Figure 2) for both micelle types over 48 h. This translates to stable R_h profiles for both micelle structures, being 16.4 ± 0.6 nm for mPP (Figure 2A inset) and 24.9 ± 1.3 nm for PPP (Figure 2B inset) after 48 h of incubation. The results agree with previous studies showing robust stabilities of other PEGylated NC types.^{44–46}

Probing PEG-Based Micelle Interactions with BSA Using PIE-FCCS. After characterizing the micelles and BSA in

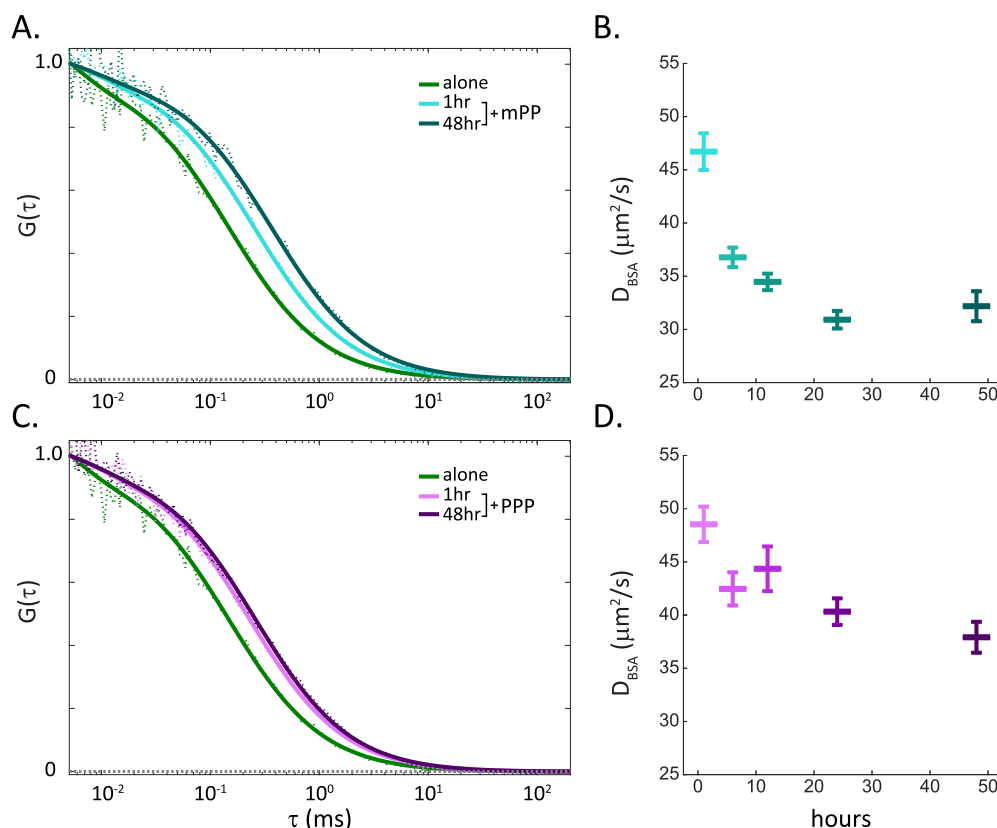


Figure 3. Time-dependent BSA co-diffusion in $1\times$ PBS. Normalized FCS correlograms of mPP (A) and PPP (B) micelle exposed BSA, respectively. The diffusion of BSA, represented here as a population-weighted average of slow and fast species, decreases when mixed with mPP (cyan) or PPP (magenta) after 1 h incubation at 37°C , indicating the presence of BSA–micelle species. Obstruction of BSA diffusion appears time-dependent, as seen by BSA correlograms after 37 $^\circ\text{C}$ incubation for 48 h with mPP (dark green) and PPP (purple). These observations are quantitatively supported by fraction-weighted averages of BSA diffusion when mixed with mPP (B) and PPP (D) after 1, 6, 12, 24, and 48 h incubation times. Error bars show the standard deviations.

isolation, we next investigated the interactions between them using two-color PIE-FCCS.⁴⁷ This technique correlates fluorescence fluctuations from both detectors as ACFs, giving diffusion and local concentration metrics for both species. In addition to the information provided by the ACFs, PIE-FCCS also produces CCF that is sensitive to correlated intensity fluctuations related to co-diffusion of the two labeled species, NR micelles and FITC-labeled BSA. PIE and TCSPC enable the removal of photons from direct excitation of NR with 488 nm light or spectral bleed-through from the FITC into the red detector.³¹ This data collection scheme avoids false-positive cross-correlation. In this way, PIE-FCCS is a rigorous indicator of the correlated diffusion of micelles and BSA and thus serves as a sensitive gauge of BSA–micelle interactions.

We prepared stock solutions of 1:1 and 1:2 ratios of micelle/BSA in $1\times$ PBS, as described in the previous section. PIE-FCCS data were recorded for each sample at the same time points as for the single-color data above: 1, 6, 12, 24, and 48 h. After 1 h, the decay times of BSA in the micelle mixture decreased significantly compared to BSA alone (Figure 3A,C). We fit the ACFs corresponding to BSA with a two-component diffusion model and plotted the population-weighted average diffusion coefficients in Figure 3B,D. Experimental diffusion coefficients for the fast and slow BSA components, representing free and micelle-bound BSA molecules, respectively, were relatively unchanged over time. The fast diffusion coefficients remained around $80\ \mu\text{m}^2/\text{s}$ for both mPP (Figure S6A) and PPP (Figure S7A) mixtures, and both BSA

concentrations, which is in good agreement with the diffusion measurements for BSA in unmixed solutions. The diffusion coefficients of the slow component species also remained consistent over time for both sets of BSA concentrations. The slow component BSA in the mPP experiments gave diffusion coefficients of around $12\ \mu\text{m}^2/\text{s}$ (Figure S6B), while those found for the PPP mixtures remained around $9\ \mu\text{m}^2/\text{s}$ (Figure S7B) for all incubation times. These differences in diffusion coefficients between micelle types of $3\ \mu\text{m}^2/\text{s}$ are in good agreement with diffusion measurements taken for the isolated micelle samples.

While the diffusion coefficients for each component showed little time dependence, the population fractions changed in a systematic way consistent with the trends in Figure 3. In the mPP micelle experiments, we found the slow component population fractions for the $1\times$ BSA mixture to be 0.323 ± 0.025 , 0.426 ± 0.008 , 0.478 ± 0.023 , 0.446 ± 0.022 , and 0.502 ± 0.027 for incubation times 1, 6, 12, 24, and 48 h, respectively, while fractions for the fast components decreased to 0.677 ± 0.025 , 0.574 ± 0.008 , 0.522 ± 0.023 , 0.554 ± 0.022 , and 0.498 ± 0.027 (Figure S6). These correlated trends in the fast and slow component populations suggest that BSA interacts directly with mPP micelles. Similar trends were observed for the triblock experiments, with slow component fractions of 0.230 ± 0.022 , 0.266 ± 0.040 , 0.308 ± 0.024 , 0.326 ± 0.025 , and 0.293 ± 0.016 , and fast population fractions of 0.770 ± 0.022 , 0.734 ± 0.040 , 0.692 ± 0.024 , 0.674 ± 0.025 , and 0.707 ± 0.016 (Figure S7). The changes

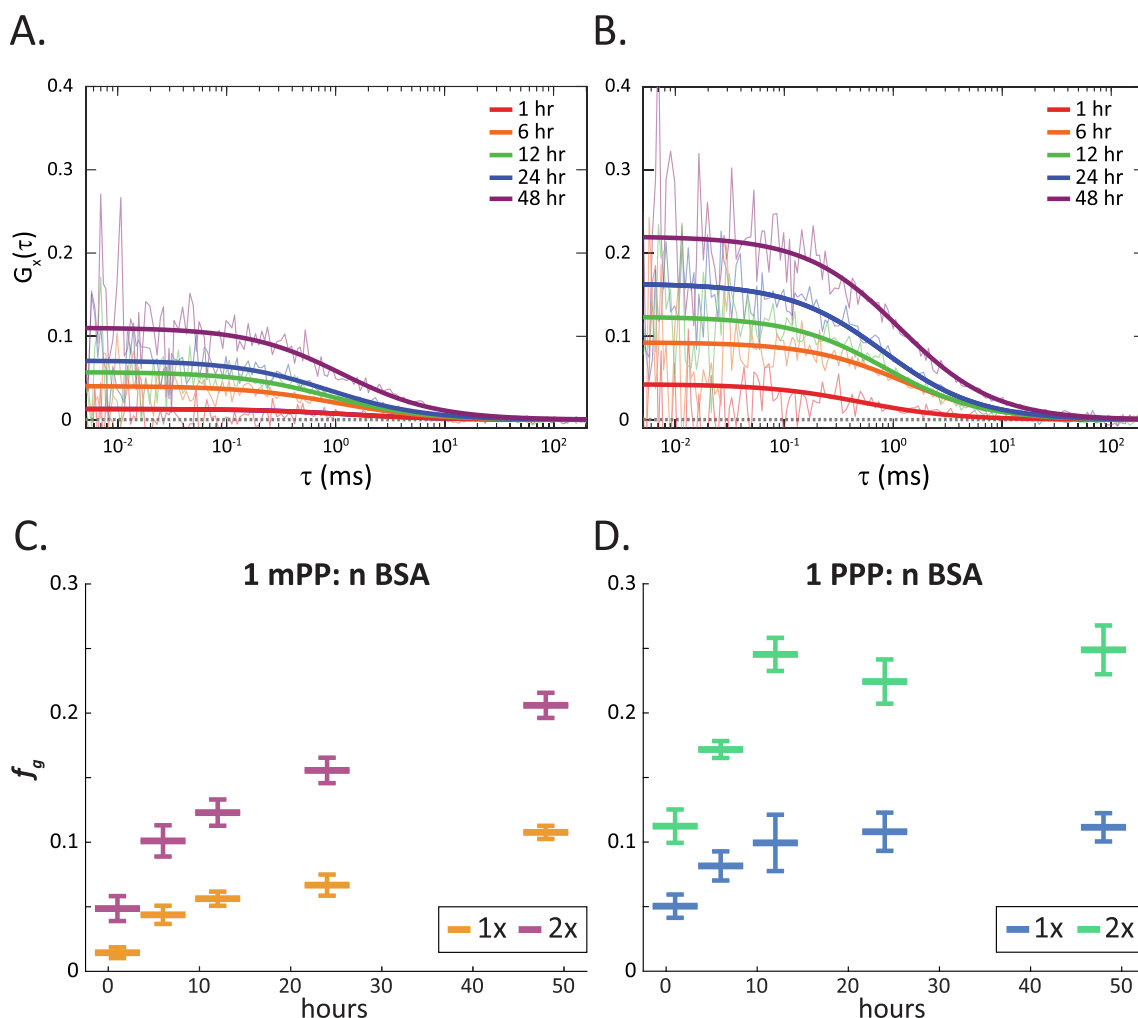


Figure 4. FCCS resolution of protein–micelle adsorption in 1× PBS. Cross-correlation functions of NR-mPP and FITC-BSA mixed at molar ratios of 1:1 (A) and 1:2 (B) for incubation times of 1, 6, 12, 24, and 48 h at 37 °C. Corresponding fraction correlated, f_g , averages for mole ratios of 1 (orange and blue) and 2× (violet and green) BSA mixed with mPP (C) and PPP (D). Error bars show the standard deviation calculated for each sample.

observed for the 2× BSA mixtures were statistically indistinguishable from those listed for the 1× mixture and can be found in Table S4. The ACF data allowed us to quantify the relative populations of slow and fast diffusing BSA-containing species suggesting a time-dependent association between BSA and micelles. To directly measure the interaction between BSA and micelle species over time, we next turned to the CCFs measured by PIE-FCCS.

The CCFs from the PIE-FCCS data are shown in Figure 4A,B. The CCFs have significant positive amplitudes, indicating co-diffusion and thus direct binding of BSA to PPP and mPP micelles. To compare the CCF amplitudes, we calculated a figure of merit, f_g , which is the ratio of the CCF amplitude to the ACF amplitude for BSA. Ranging from 0 to 1, the magnitude of f_g is proportional to the fraction of BSA bound to micelles. Results from mPP experiments show that after 1 h of incubation, f_g is 0.014 ± 0.004 for a 1:1 ratio of BSA to micelles and 0.05 ± 0.01 for a 2:1 ratio of BSA to micelles. After 48 h of incubation, the fraction of bound BSA increases to 0.108 ± 0.005 and 0.21 ± 0.01 , respectively (Figure 4C). This indicates weak binding of the protein to micelles. This conclusion is consistent with the observation that the diffusion coefficients and R_h values of BSA never reach

those of the micelles even after 48 h of incubation, which also suggests incomplete binding.

For PPP-containing mixtures, at time points 1 and 48 h, the f_g values increase from 0.050 ± 0.009 to 0.11 ± 0.01 , and 0.11 ± 0.01 to 0.25 ± 0.02 for BSA mole ratios of 1 and 2, respectively (Figure 4D). The endpoint f_g values were nearly identical for mPP and PPP for the 1× BSA mixtures. For the 2× BSA mixtures, the endpoint f_g value for PPP was higher than that for mPP (0.25 vs 0.21). Additionally, the PPP mixtures reached a maximum f_g after 10 h of incubation, indicating faster binding.

To better understand the f_g values, we used a probabilistic model that considers the effects of micelle/BSA ratio differences between experiments, in combination with a mathematical framework presented previously in the group.³¹ We found that none of the f_g values in Figure 4 were consistent with micelle–BSA binding above 50%. Specifically, the mPP and PPP were incubated for 48 h with 1× BSA had f_g values consistent with 22 and 19% binding, respectively. The micelle–BSA population increased to 39 and 46% when mPP and PPP were incubated for 48 h with 2× BSA, respectively. These results support the conclusion that BSA

binds more strongly to PPP micelles compared to mPP micelles.

CONCLUSIONS

In this study, we characterized the stability and protein adsorption of two PEG-based block copolymer micelles to compare the effects of PEG architecture on BSA–micelle interactions. Both micelles demonstrated reasonable stability, as indicated by their consistent sizes through changes in temperature, chemical environment, and time. FCS data showed that BSA diffusion slows significantly when mixed equimolarly with either micelle, with both demonstrating similar time dependencies. However, similar mixtures containing double the original BSA concentrations showed diffusion coefficients indistinguishable from those of the equimolar samples. FCCS measurements indicated a time dependence of the BSA–micelle interactions as well as a dependence on BSA concentration, with PPP mixtures displaying slightly faster and stronger BSA binding compared to mPP. These results illustrate the utility of cross-correlation-based metrics for studying binding affinities rather than purely FCS-based measurements, as the latter can be complicated by the number of differently sized fluorescent species in a measured system.

Many studies have shown the advantages of using FCS to measure NC stabilities or reactivities when titrated with various serum proteins.^{48–51} While these studies provide invaluable insights for non-PEGylated and solid NCs, the field lacks studies for PEGylated micellar systems, which are currently being explored for hydrophobic drug delivery. Additionally, these studies often rely on exceptionally small NCs and high protein concentrations to register discernible changes in the NC hydrodynamic radii following incubation with proteins. It should be noted that recent work has employed PIE-FCCS to measure the effects of various polymer coatings on protein binding to MOF nanoparticles (NPs), demonstrating the ability to detect their relatively strong interactions with globulin species.²⁸ However, this methodology cannot be extended to the micellar system as there are distinct differences in the composition of the solution. For example, MOF NPs are homogenous as they are frozen assemblies with the dyes locked inside the core. Micelles are in a dynamic environment that will simultaneously contain micelles, free polymers, and free dye. Thus, there is a need to develop a method by which dynamic assemblies can be studied with PIE-FCCS.

This study suggests that single-color FCS can be used to detect BSA interactions with PEGylated micelles, but it alone does not provide enough information about the magnitudes of such interactions to resolve binding affinity differences between a linear and cyclic PEGylated micelle corona. Further, the stoichiometric influences on binding affinities were indiscernible from the FCS data alone when using BSA at relatively low concentrations. PIE-FCCS, on the other hand, does resolve the time dependence of micelle–BSA interactions and distinguishes the effect of BSA stoichiometry on average micelle–BSA aggregation. Our approach was able to resolve differences in binding based on the architecture of (m)PEG-PCL-based micelles.

The results reported above were consistent with our expectations that the difference in binding affinity between the two architectures would be small and, therefore, have a slight change in an already low concentration of co-diffusing species. However, we did not expect that the cyclic PPP

micelles would have a higher binding affinity for BSA. Because the architecture of the mPP contains a methyl end group, we anticipated that the methyl end groups would form hydrophobic pockets on the surface of the micelles, leading to more nonspecific interactions with BSA. By cyclizing the PEG, we essentially remove the methyl end groups, thereby avoiding the expected hydrophobic pockets. One possible explanation for the unexpected result is that the surface topology of the cyclized PEG creates an electrostatic environment that has a higher affinity for BSA as the end of a cyclized PEG resembles that of a crown ether. In fact, cations have been used as templates to encourage PEG folding in cyclization reactions.⁵² If the PEG remains chelated with the K^+ and Na^+ contained in the $1\times$ PBS, the resulting ions may cause charges to form on the micelles surface, leading to interactions with the negatively charged BSA at a pH of 7.4.

Further work is needed to resolve the surface binding properties of the PEG-based micelles explored in this study. Here, we demonstrated the value of PIE-FCCS to study protein binding at low concentrations for a micelle system that was thought to be “stealthy” and elude non-specific protein interaction. Our approach made it possible to measure small differences in binding affinity and discover an unexpected difference in the surface environment of the micelles. Future work could further reveal the binding affinity between PEGylated micelles in the presence of other common serum proteins involved in PEG immune responses. Quantitative fluorescence assays, as presented here, could make it possible to elucidate the mechanism of the ABC phenomenon and determine why this immune response occurs with some PEGylated systems but not others.

ASSOCIATED CONTENT

Supporting Information

The Supporting Information is available free of charge at <https://pubs.acs.org/doi/10.1021/acs.biomac.2c01538>.

Methods, polymer and micelle characterization results, additional FCS data, dilution calculations, and data tables (PDF)

AUTHOR INFORMATION

Corresponding Author

Adam W. Smith – Department of Chemistry, University of Akron, Akron, Ohio 44325, United States; Department of Chemistry and Biochemistry, Texas Tech University, Lubbock, Texas 79410, United States; orcid.org/0000-0001-5216-9017; Email: aw.smith@ttu.edu

Authors

D. Paul Mallory – Department of Chemistry, University of Akron, Akron, Ohio 44325, United States

Abegel Freedman – School of Polymer Science and Polymer Engineering, University of Akron, Akron, Ohio 44325, United States; Department of Chemistry and Biochemistry, Wichita State University, Wichita, Kansas 67260, United States

Megan J. Kaliszewski – Department of Chemistry, University of Akron, Akron, Ohio 44325, United States

Gladys Rocío Montenegro-Galindo – School of Polymer Science and Polymer Engineering, University of Akron, Akron, Ohio 44325, United States

Coleen Pugh – School of Polymer Science and Polymer Engineering, University of Akron, Akron, Ohio 44325, United States

States; Department of Chemistry and Biochemistry, Wichita State University, Wichita, Kansas 67260, United States; orcid.org/0000-0002-1476-0890

Complete contact information is available at: <https://pubs.acs.org/10.1021/acs.biomac.2c01538>

Author Contributions

¹D.P.M. and A.F. contributed equally to this work.

Notes

The authors declare no competing financial interest.

ACKNOWLEDGMENTS

This work was supported by funding from the National Science Foundation under grant number CHE-1753060. We also acknowledge partial support from the University of Akron Graduate School and Department of Polymer Science as well as Wichita State University Start-up Funds.

REFERENCES

- (1) Lin, W. J.; Juang, L. W.; Wang, C. L.; Chen, Y. C.; Lin, C. C.; Chang, K. L. Pegylated Polyester Polymeric Micelles as a Nano-carrier: Synthesis, Characterization, Degradation, and Biodistribution. *J. Exp. Clin. Med.* **2010**, *2*, 4–10.
- (2) Shi, B.; Fang, C.; You, M. X.; Zhang, Y.; Fu, S.; Pei, Y. Y. Stealth MePEG-PCL micelles: Effects of polymer composition on micelle physicochemical characteristics, in vitro drug release, in vivo pharmacokinetics in rats and biodistribution in S180 tumor bearing mice. *Colloid Polym. Sci.* **2005**, *283*, 954–967.
- (3) Danafar, H. Study of the Composition of Polycaprolactone/Poly (Ethylene Glycol)/Polycaprolactone Copolymer and Drug-to-Polymer Ratio on Drug Loading Efficiency of Curcumin to Nanoparticles. *Jundishapur J. Nat. Pharm. Prod* **2016**, *12*, 1–9.
- (4) Mosqueira, V. C. F.; Legrand, P.; Morgat, J. L.; Vert, M.; Mysiakine, E.; Gref, R.; Devissaguet, J. P.; Barratt, G. Biodistribution of long-circulating PEG-grafted nanocapsules in mice: Effects of PEG chain length and density. *Pharm. Res.* **2001**, *18*, 1411–1419.
- (5) Ukawala, M.; Rajyaguru, T.; Chaudhari, K.; Manjappa, A. S.; Pimple, S.; Babbar, A. K.; Mathur, R.; Mishra, A. K.; Murthy, R. S. R. Investigation on design of stable etoposide-loaded PEG-PCL micelles: Effect of molecular weight of PEG-PCL diblock copolymer on the in vitro and in vivo performance of micelles. *Drug Delivery* **2012**, *19*, 155–167.
- (6) Wang, Q.; Jiang, J.; Chen, W.; Jiang, H.; Zhang, Z.; Sun, X. Targeted delivery of low-dose dexamethasone using PCL-PEG micelles for effective treatment of rheumatoid arthritis. *J. Controlled Release* **2016**, *230*, 64–72.
- (7) Lin, W. J.; Chen, Y. C.; Lin, C. C.; Chen, C. F.; Chen, J. W. Characterization of pegylated copolymeric micelles and in vivo pharmacokinetics and biodistribution studies. *J. Biomed. Mater. Res., Part B* **2006**, *77B*, 188–194.
- (8) Dams, E. T. M.; Laverman, P.; Oyen, W. J. G.; Storm, G.; Scherphof, G. L.; Van Der Meer, J. W. M.; Corstens, F. H. M.; Boerman, O. C. Accelerated blood clearance and altered biodistribution of repeated injections of sterically stabilized liposomes. *J. Pharmacol. Exp. Ther.* **2000**, *292*, 1071–1079.
- (9) Su, Y.; Liu, M.; Xiong, Y.; Ding, J.; Liu, X.; Song, Y.; Deng, Y. Effects of stability of PEGylated micelles on the accelerated blood clearance phenomenon. *Drug Delivery Transl. Res.* **2019**, *9*, 66–75.
- (10) Shiraishi, K.; Hamano, M.; Ma, H.; Kawano, K.; Maitani, Y.; Aoshi, T.; Ishii, K. J.; Yokoyama, M. Hydrophobic blocks of PEG-conjugates play a significant role in the accelerated blood clearance (ABC) phenomenon. *J. Controlled Release* **2013**, *165*, 183–190.
- (11) Koide, H.; Asai, T.; Kato, H.; Ando, H.; Shiraishi, K.; Yokoyama, M.; Oku, N. Size-dependent induction of accelerated blood clearance phenomenon by repeated injections of polymeric micelles. *Int. J. Pharm.* **2012**, *432*, 75–79.
- (12) Kozma, G. T.; Shimizu, T.; Ishida, T.; Szebeni, J. Anti-PEG antibodies: Properties, formation, testing and role in adverse immune reactions to PEGylated nano-biopharmaceuticals. *Adv. Drug Delivery Rev.* **2020**, *154–155*, 163–175.
- (13) Cheng, X.; Wang, C.; Su, Y.; Luo, X.; Liu, X.; Song, Y.; Deng, Y. Enhanced Opsonization-Independent Phagocytosis and High Response Ability to Opsonized Antigen-Antibody Complexes: A New Role of Kupffer Cells in the Accelerated Blood Clearance Phenomenon upon Repeated Injection of PEGylated Emulsions. *Mol. Pharm.* **2018**, *15*, 3755–3766.
- (14) Chanan-Khan, A.; Szebeni, J.; Savay, S.; Liebes, L.; Rafique, N. M.; Alving, C. R.; Muggia, F. M. Complement activation following first exposure to pegylated liposomal doxorubicin (Doxil®): Possible role in hypersensitivity reactions. *Ann. Oncol.* **2003**, *14*, 1430–1437.
- (15) Hashimoto, Y.; Shimizu, T.; Mima, Y.; Abu Lila, A. S.; Ishida, T.; Kiwada, H. Generation, characterization and in vivo biological activity of two distinct monoclonal anti-PEG IgMs. *Toxicol. Appl. Pharmacol.* **2014**, *277*, 30–38.
- (16) Shimizu, T.; Abu Lila, A. S.; Fujita, R.; Awata, M.; Kawanishi, M.; Hashimoto, Y.; Okuhira, K.; Ishida, Y.; Ishida, T. A hydroxyl PEG version of PEGylated liposomes and its impact on anti-PEG IgM induction and on the accelerated clearance of PEGylated liposomes. *Eur. J. Pharm. Biopharm.* **2018**, *127*, 142–149.
- (17) Hong, L.; Wang, Z.; Wei, X.; Shi, J.; Li, C. Antibodies against polyethylene glycol in human blood: A literature review. *J. Pharmacol. Toxicol. Methods* **2020**, *102*, 106678.
- (18) Shiraishi, K.; Yokoyama, M. Polymeric micelles possessing polyethyleneglycol as outer shell and their unique behaviors in accelerated blood clearance phenomenon. *Biol. Pharm. Bull.* **2013**, *36*, 878–882.
- (19) Ma, H.; Shiraishi, K.; Minowa, T.; Kawano, K.; Yokoyama, M.; Hattori, Y.; Maitani, Y. Accelerated Blood Clearance Was Not Induced for a Gadolinium-Containing PEG-poly(L-lysine)-Based Polymeric Micelle in Mice. *Pharm. Res.* **2010**, *27*, 296–302.
- (20) Shiraishi, K.; Yokoyama, M. Toxicity and immunogenicity concerns related to PEGylated-micelle carrier systems: a review. *Sci. Technol. Adv. Mater.* **2019**, *20*, 324–336.
- (21) Wan, Y.; Gan, Z.; Li, Z. Effects of the surface charge on the stability of PEG-b-PCL micelles: Simulation of the interactions between charged micelles and plasma components. *Polym. Chem.* **2014**, *5*, 1720–1727.
- (22) Liu, J.; Zeng, F.; Allen, C. In vivo fate of unimers and micelles of a poly(ethylene glycol)-block-poly(caprolactone) copolymer in mice following intravenous administration. *Eur. J. Pharm. Biopharm.* **2007**, *65*, 309–319.
- (23) Magde, D.; Elson, E.; Webb, W. W. Thermodynamic Fluctuations in a Reacting System—Measurement by Fluorescence Correlation Spectroscopy. *Phys. Rev. Lett.* **1972**, *29*, 705–708.
- (24) Kristensen, K.; Urquhart, A. J.; Thormann, E.; Andresen, T. L. Binding of human serum albumin to PEGylated liposomes: insights into binding numbers and dynamics by fluorescence correlation spectroscopy. *Nanoscale* **2016**, *8*, 19726–19736.
- (25) Eriksen, A. Z.; Brewer, J.; Andresen, T. L.; Urquhart, A. J. The diffusion dynamics of PEGylated liposomes in the intact vitreous of the ex vivo porcine eye: A fluorescence correlation spectroscopy and biodistribution study. *Int. J. Pharm.* **2017**, *S22*, 90–97.
- (26) Digman, M. A.; Gratton, E. Lessons in Fluctuation Correlation Spectroscopy. *Annu. Rev. Phys. Chem.* **2011**, *62*, 645–668.
- (27) Bacia, K.; Schwille, P. Practical guidelines for dual-color fluorescence cross-correlation spectroscopy. *Nat. Protoc.* **2007**, *2*, 2842–2856.
- (28) Zimpel, A.; Al Danaf, N.; Steinborn, B.; Kuhn, J.; Höhn, M.; Bauer, T.; Hirschle, P.; Schrimpf, W.; Engelke, H.; Wagner, E.; Barz, M.; Lamb, D. C.; Lächelt, U.; Wuttke, S. Coordinative Binding of Polymers to Metal–Organic Framework Nanoparticles for Control of Interactions at the Biointerface. *ACS Nano* **2019**, *13*, 3884–3895.
- (29) Kowalski, A.; Duda, A.; Penczek, S. Kinetics and Mechanism of Cyclic Esters Polymerization Initiated with Tin(II) Octoate. 3. Polymerization of L,L-Dilactide. *Macromolecules* **2000**, *33*, 7359–7370.

- (30) Aliabadi, H. M.; Elhasi, S.; Mahmud, A.; Gulamhusein, R.; Mahdipour, P.; Lavasanifar, A. Encapsulation of hydrophobic drugs in polymeric micelles through co-solvent evaporation: The effect of solvent composition on micellar properties and drug loading. *Int. J. Pharm.* **2007**, *329*, 158–165.
- (31) Kaliszewski, M. J.; Shi, X.; Hou, Y.; Lingerak, R.; Kim, S.; Mallory, P.; Smith, A. W. Quantifying membrane protein oligomerization with fluorescence cross-correlation spectroscopy. *Methods* **2018**, *140–141*, 40–51.
- (32) Comar, W. D.; Schubert, S. M.; Jastrzebska, B.; Palczewski, K.; Smith, A. W. Time-Resolved Fluorescence Spectroscopy Measures Clustering and Mobility of a G Protein-Coupled Receptor Opsin in Live Cell Membranes. *J. Am. Chem. Soc.* **2014**, *136*, 8342–8349.
- (33) Schrimpf, W.; Barth, A.; Hendrix, J.; Lamb, D. C. P. A. M. PAM: A Framework for Integrated Analysis of Imaging, Single-Molecule, and Ensemble Fluorescence Data. *Biophys. J.* **2018**, *114*, 1518–1528.
- (34) Pabbathi, A.; Patra, S.; Samanta, A. Structural Transformation of Bovine Serum Albumin Induced by Dimethyl Sulfoxide and Probed by Fluorescence Correlation Spectroscopy and Additional Methods. *Chemphyschem* **2013**, *14*, 2441–2449.
- (35) Tran, T. Q. M.; Hsieh, M. F.; Chang, K. L.; Pho, Q. H.; Nguyen, V. C.; Cheng, C. Y.; Huang, C. M. Bactericidal effect of lauric Acid-Loaded PCL-PEG-PCL nano-sized micelles on skin commensal propionibacterium acnes. *Polymers* **2016**, *8*, 321.
- (36) Tyrrell, Z. L.; Shen, Y.; Radosz, M. Near-critical fluid micellization for high and efficient drug loading: Encapsulation of paclitaxel into PEG-b-PCL micelles. *J. Phys. Chem. C* **2011**, *115*, 11951–11956.
- (37) Gendron, P.; Avaltroni, F.; Wilkinson, K. J. Diffusion Coefficients of Several Rhodamine Derivatives as Determined by Pulsed Field Gradient – Nuclear Magnetic Resonance and Fluorescence Correlation Spectroscopy. *J. Fluoresc.* **2008**, *18*, 1093–1101.
- (38) Luschtinetz, F.; Dosche, C. Determination of micelle diffusion coefficients with fluorescence correlation spectroscopy (FCS). *J. Colloid Interface Sci.* **2009**, *338*, 312–315.
- (39) Kurniasih, I. N.; Liang, H.; Mohr, P. C.; Khot, G.; Rabe, J. P.; Mohr, A. Nile Red Dye in Aqueous Surfactant and Micellar Solution. *Langmuir* **2015**, *31*, 2639–2648.
- (40) Shuai, X.; Ai, H.; Nasongkla, N.; Kim, S.; Gao, J. Micellar carriers based on block copolymers of poly(ϵ -caprolactone) and poly(ethylene glycol) for doxorubicin delivery. *J. Controlled Release* **2004**, *98*, 415–426.
- (41) Hu, Y.; Xie, J.; Tong, Y. W.; Wang, C.-H. Effect of PEG conformation and particle size on the cellular uptake efficiency of nanoparticles with the HepG2 cells. *J. Controlled Release* **2007**, *118*, 7–17.
- (42) Zhang, X.; Poniewierski, A.; Hou, S.; Sozański, K.; Wisniewska, A.; Wieczorek, S. A.; Kalwarczyk, T.; Sun, L.; Holyst, R. Tracking structural transitions of bovine serum albumin in surfactant solutions by fluorescence correlation spectroscopy and fluorescence lifetime analysis. *Soft Matter* **2015**, *11*, 2512–2518.
- (43) Lee, H.; Larson, R. G. Adsorption of plasma proteins onto PEGylated lipid bilayers: the effect of PEG size and grafting density. *Biomacromolecules* **2016**, *17*, 1757–1765.
- (44) Hsu, H.-j.; Han, Y.; Cheong, M.; Král, P.; Hong, S. Dendritic PEG outer shells enhance serum stability of polymeric micelles. *Nanomedicine* **2018**, *14*, 1879–1889.
- (45) Feiner-gracia, N.; Buzhor, M.; Fuentes, E.; Pujals, S.; Amir, R. J.; Albertazzi, L. Micellar Stability in Biological Media Dictates Internalization in Living Cells. *J. Am. Chem. Soc.* **2017**, *139*, 16677–16687.
- (46) Kareem, F.; Bhayo, A. M.; Imran, M.; Shah, M. R.; Khan, K. M.; Malik, M. I. Enhanced therapeutic efficacy of clotrimazole by delivery through poly(ethylene oxide)-block-poly (ϵ -caprolactone) copolymer-based micelles. *J. Appl. Polym. Sci.* **2019**, *136*, 47769.
- (47) Müller, B. K.; Zaychikov, E.; Bräuchle, C.; Lamb, D. C. Pulsed Interleaved Excitation. *Biophys. J.* **2005**, *89*, 3508–3522.
- (48) Milani, S.; Baldelli Bombelli, F.; Pitek, A. S.; Dawson, K. A.; Rädler, J. Reversible versus irreversible binding of transferrin to polystyrene nanoparticles: Soft and hard corona. *ACS Nano* **2012**, *6*, 2532–2541.
- (49) Wang, H.; Lin, Y.; Nienhaus, K.; Nienhaus, G. U. The protein corona on nanoparticles as viewed from a nanoparticle-sizing perspective. *Wiley Interdiscip. Rev.: Nanomed. Nanobiotechnol.* **2018**, *10*, No. e1500.
- (50) Zhang, X.; Poniewierski, A.; Jelińska, A.; Zagodzón, A.; Wisniewska, A.; Hou, S.; Holyst, R. Determination of equilibrium and rate constants for complex formation by fluorescence correlation spectroscopy supplemented by dynamic light scattering and Taylor dispersion analysis. *Soft Matter* **2016**, *12*, 8186–8194.
- (51) Wang, H.; Ma, R.; Nienhaus, K.; Nienhaus, G. U. Formation of a Monolayer Protein Corona around Polystyrene Nanoparticles and Implications for Nanoparticle Agglomeration. *Small* **2019**, *15*, 1900974.
- (52) Elliott, B. J.; Willis, W. B.; Bowman, C. N. Polymerization Kinetics of Pseudocrown Ether Network Formation for Facilitated Transport Membranes. *Macromolecules* **1999**, *32*, 3201–3208.

Recommended by ACS

Effects of Immune Cell Heterogeneity and Protein Corona on the Cellular Association and Cytotoxicity of Gold Nanoparticles: A Single-Cell-Based, High-Dimensional Ma...

Sehee Park, Tae Hyun Yoon, *et al.*

APRIL 24, 2023
ACS NANOSCIENCE AU

READ 

Single-Particle Functionality Imaging of Antibody-Conjugated Nanoparticles in Complex Media

Laura Woythe, Lorenzo Albertazzi, *et al.*

JANUARY 03, 2023
ACS APPLIED BIO MATERIALS

READ 

Size-Dependent Polymeric Nanoparticle Distribution in a Static versus Dynamic Microfluidic Blood Vessel Model: Implications for Nanoparticle-Based Drug Delivery

Sara Gimondi, Nuno M. Neves, *et al.*

APRIL 24, 2023
ACS APPLIED NANO MATERIALS

READ 

Multicolor Super-Resolution Microscopy of Protein Corona on Single Nanoparticles

Yuyang Wang, Lorenzo Albertazzi, *et al.*

AUGUST 12, 2022
ACS APPLIED MATERIALS & INTERFACES

READ 

Get More Suggestions >